

CrystEngComm

COMMUNICATION

In situ visualization of superior nanomechanical flexibility of individual hydroxyapatite nanobelts

Received 00th January 20xx, Accepted 00th January 20xx

DOI: 10.1039/x0xx00000x

www.rsc.org/

Mei-li Qi, a,b,c Zhen-nan Huang, Wen-tao Yao, Fei Long, Meng Cheng, Bo-ao Song, David Banner, Reza Shahbazian-Yassar, Yu-peng Lua,b* and Tolou Shokuhfar

Highly flexible multi-layered hydroxyapatite (HA) nanobelts were successfully grown and compared to nanorods. Nanomechanical behaviour of individual HA nanostructures was visualized using *in situ* TEM. Compression-induced deformation in HA nanobelts can spontaneously recover at a maximal strain of 99.2%, much larger than the 2.63% failure strain observed for traditional HA nanorods.

The biocompatibility, bioactivity, osteoconductivity and nontoxic properties of synthetic hydroxyapatite (HA) with controlled sizes and morphologies are ideal in bone repair, tissue engineering, drug delivery, and related applications.^{1, 2} However, the brittleness and poor fatigue resistance of synthetic HA greatly limits its applications for load-bearing materials.3, 4 Molten salt,⁵ hydrothermal,⁶ electrospinning⁸ and electroblowing⁹ methods were developed to synthesize flexible HA structures. 10, 11 However, synthesizing HA nanostructures with uniform morphology and high aspect ratio (>100) is still an experimental challenge. Measuring the flexibility of synthesized HA and the corresponding flexion mechanisms present additional technical challenges. Flexibility has been mainly described through bent morphology, static microstructures, or macroscopic tensile testing. 12, 13 These methods, however, cannot provide direct observation of the microscopic structure alternations in real-time and only infer the flexibility mechanism. It is of crucial importance to identify whether the HA structures with bending phenomenon is flexible.

In this communication, flexible multi-layered HA nanobelts and traditional nanorods with uniform morphology and high aspect ratios were synthesized by a one-step hydrothermal homogeneous precipitation method. For the first time, the real-time deformation process of individual HA nanostructures was visualized via *in situ* transmission electron microscopy (TEM). Atomic force microscope (AFM) nanoindentation tests showed that the HA nanobelts possess a better resistance to the tip indentation and a more reduced modulus.

The aqueous solutions of Ca(NO₃)₂·4H₂O, (NH₄)₂HPO₄, and 1 M urea/acetamide were mixed with a 1.67 Ca/P molar ratio. The pH values of the above solutions were then adjusted to 3.5 using 0.5 M HNO_{3(aq)}. After that, the solutions were transferred to 100 ml Tefloncylindrical stainless steel autoclave reactors hydrothermally treated at 160°C for 6 h in an oven. Finally, the obtained products were collected and washed with deionized water and anhydrous ethanol, and dried at 80°C. The morphology of the synthesized products was characterized by field emission scanning electron microscopy (FE-SEM, SU-70). The product synthesized with a urea pH regulator formed uniform belt-like nanostructures with a width of 500-1000 nm and a thickness of 50-100 nm [Fig. 1(a)], while the product synthesized with acetamide as a pH regulator formed rod-like nanostructures with a diameter of 500-1000 nm [Fig. 1(b)]. The nanobelts are highly transparent to electrons even when overlapped, suggesting that they are very thin. Both the nanobelt and nanorod have high aspect ratios [Fig. 1(a-b)] and suggest preferential orientation growth of our nanostructures. All observed XRD peaks are in accordance with the HA standard database (JCPDS card 09-0432) and confirm the samples are HA [Fig. 1(c-d)]. The strongest XRD peak intensity shifts from (211) to (300), compared with the HA standard database. Further TEM study of individual nanobelt and nanorod [Fig. 1(a-b)] are shown in [Fig. 1(e-f)]. The corresponding selected area electron diffraction (SAED) patterns in the inset panel indicate singlecrystalline nature of individual nanobelt and nanorod. By comparing the orientation of the HA nanostructures [Fig. 1(e-f)] with the orientation of Single Crystal and Crystal Maker

E-mail address: biosdu@sdu.edu.cn, rsyassar@uic.edu.

Electronic Supplementary Information (ESI) available: See DOI: 10.1039/x0xx00000x

^a Key Laboratory for Liquid-Solid Structural Evolution and Processing of Materials, Ministry of Education, Shandong University, Ji'nan, 250061, China.

b. School of Materials Science and Engineering, Shandong University, Ji'nan, 250061, China.

^{c.} Department of Mechanical and Industrial Engineering, University of Illinois at Chicago, Chicago, Illinois 60607, United States.

^d Department of Mechanical Engineering-Engineering Mechanics, Michigan Technological University, Houghton, Michigan 49931, United States.

e- Department of Bioengineering, University of Illinois at Chicago, Chicago, Illinois 60607, United States

COMMUNICATION CrystEngComm

simulations, the priority growth direction of the synthesized nanostructures is confirmed to be along the [001] direction [Fig. 1(g-h)]. In addition, the formation of HA nanobelts under experimental conditions indicate a difference of the growth rates along the thickness direction and the width direction, which are both perpendicular to the [100] growth direction.

Different pH regulators could influence HA nanostructures via influencing the hydrothermal reaction rate. For the formation of HA nanobelts, urea was used as the pH regulator, wherein the pH 8.77 in the final reaction solutions. During the synthesizing process, urea release hydroxyl quickly and continuously. The alkaline environment and continual release of hydroxyl may ensure the HA nanostructures always grow along the priority [001] direction to form the HA nanobelts. However, the acetamide produced HA nanorods with a final pH of 4.33. The release of the hydroxyl is very slow, which slows the growth rate of HA nanostructure. Therefore, other than the priority growth direction, the HA nanostructure may also grow along other directions slowly. This leads to the formation of HA nanorods.

Recently, *in situ* transmission electron microscopy (TEM) has been used as an effective tool for direct measurement of an individual structure such as TiO₂ nanotubes¹⁴, shear-exfoliated phosphorene nanowires¹⁵ and graphene ribbons.¹⁶ This electron microscopy (EM) approach measures the properties of individual structures and records structural changes during loading through advanced electron imaging and diffraction techniques, providing an ideal experimental setup for the dynamic study of nanoscale property-structure relationships.

Here, in situ nanomechanical properties of individual HA nanostructures were performed with a JEOL 3010 TEM operated at 300 KeV using an in situ Nanofactory sample holder. The holder is equipped with a piezo-tube driven manipulator to control movement [ESI1 Fig. S1(a)†]. A chemically etched tungsten (W) tip is mounted onto the movable manipulator that can be driven along X, Y, and Z directions with nanoscale precision. ESI1 Fig. 1(b)† is a low magnified TEM image showing the W electrode tip, Au wire and a selected HA nanostructure with enlarged image of the contact area shown in [ESI1 Fig. 1(c)†]. Individual HA nanostructures were attached to the edge of the counterpart Au wire, which was put onto the fixed terminal facing the W probe. The W tip was then fixed on a copper hat, which sat on the sapphire ball. By manipulating the W tip in 3D, the bending, scrolling, and stretching of the HA nanostructures were captured and recorded.

The HA nanobelt was subjected to seven continuous cycles of compression tests without any morphology change or cracks formed inside the structure (ESI2 Movie†). According to the conventional equation, 17 ϵ = r/(r+R)%, the elastic strain-compression time curve during the seventh compression process is shown in Fig. 2f, where R is the compression curvature and r refers to the thickness of the nanobelt and the radius of the nanorod. The value R decreased during the compression experiments. Therefore, the strain ϵ can be increased to a maximum value. Detailed information about the calculation of the elastic strain can be found in ESI1 Fig. S2†. *In situ* TEM snapshot progress with compression angles and

calculated strain of an individual HA nanobelt in the first five compression-recovery cycles can be found in ESI1 Fig. S3[†]. The nanobelt recovered to its original state of each of those compression-bending trials. In the seventh cycle [Fig. 3(a-e)], the distorted compression angle even approached 180°. At 180° distortion, the value of R can be considered to approximately 0. According to the above formula, $\varepsilon \approx 100\%$. More interestingly, the nanobelt still recovered from this extreme angle upon releasing the applied compression force. After seven compression tests, the HA nanobelt kept its original morphology with only 0.8% strain, which indicates its outstanding structural stability and deformation resistance under external compression forces. The HA nanobelt survived without detectable cracking or morphological change and remained flat during and after the compression. To our knowledge, this is the first observation of the unique flexibility of an individual HA nanobelt.

To investigate on the possible structure difference before and after the compression, SAED patterns were analysed (ESI1 Fig. S4†). According to literature, SAED patterns has been used in the mechanical testing of nanobelts for the determination of strain. 18 Due to the uniformity in the strain, there should be systematic changes in the diffraction pattern. 19 Deforming the crystal can lead to strain, and thus the SAED patterns are influenced through intensity variations and additional satellite spots.²⁰ Here, the SAED patterns before and after the seventh cycle of severe compression test reflect the typical single crystal of HA and were indexed to [120] zone axis. Only several extinction spots appeared in the final SAED patterns, which can be related to the residual stress and the geometrical changes of the lattice structure. 19 The result is in accordance with the remaining 0.8% strain after the seventh compression. Such SAED patterns are associated with the process of structural recovery.

Serial images captured in situ of the original [Fig. 2(h)], bent [Fig. 2(i-k)] and fractured [Fig. 2(I)] states of a representative HA nanorod were also shown. Details can be found in ESI3 Movie†. The nanorod experienced a compression process when the load was applied. At this deformation process, we observed a crackinitiated failure. The corresponding strain-compression time curve during this process is shown in Fig. 2(m). The HA nanorod broke when strain ϵ exceed ~2.63% at 12.7 s. The HA nanorod failed in an abrupt and catastrophic manner without any observable necking process upon further compression [Fig. 2(k-I)]. The angle of inclination does not change between the original and final states of the nanorod (Fig. S6). This unaltered angle of inclination is additional evidence of the fraction behaviour of the nanorod. Besides, the fracture behaviour is a common feature of the nanorod. Details of the compression test of another typical nanorod was shown in ESI4 Movie†. The TEM images of the nanorod taken before and after the compression test were shown in Fig. S7 a and c. High magnification TEM images of the nanorod's top and fractured region were shown in Fig. S7 b and d. From these results, it is concluded that the fracture form belongs to brittle fracture. During the compression process, the stress would be concentrated to one point, and the nanorod reached its elastic CrystEngComm COMMUNICATION

limit instead of undergoing plastic deformation. The nanorod therefore exhibited a brittle failure fracture.

To further investigate the reduced modulus of these two nanostructures, AFM nanoindentation experiments were carried out with Dimension ICON system (Bruker, CA) in ambient conditions. The nanobelt and nanorod samples were dispersed in 99% ethanol, and then deposited on freshly cleaved mica substrate. DNISP nanoindentation cantilever (Bruker, CA) was employed for the indentation tests. The Oliver-Pharr method was utilized to calibrate the instrument and analyze the experimental data.²¹⁻²³ The elasticity modulus was computed from the suggested formulas by Sneddon. 24, 25 Three indentations on the randomly chosen sites of the two samples were conducted. Representative force vs displacement curves obtained from nanoindentation test together with the surface morphology of the nanobelt and nanorod taken before and after the experiment in AFM are shown in Fig. 3. The aspect ratio of the cross-section profile (height/width) was 0.17 for the nanobelt. The aspect ratio of the cross-section profile of the nanorod was 0.64, close to the value of 0.86 for a perfect hexagonal structure (inset images in Fig. 3). The indentation depth for the nanobelt was 12 nm to 15 nm, which is less than 10% of the sample thickness. However, the indentation depth was difficult to determine for the nanorod due to fracture failure during testing. Therefore, the hexagonal nanorod exhibited more brittleness, which also can be seen from the topography image that cracks propagate along the vertical indentation direction. The measured reduced modulus E* for the nanobelt was 97.6 GPa, two times larger than that of the nanorod (E*=41.5 GPa). This also confirms the flexible behavior of the nanobelt.

To reveal the flexural failure mechanism of the HA nanostructures, a schematic diagram of the nanorod, singlelayered nanobelt and multi-layered nanobelt during deformation is illustrated in Fig. 4. While applied stress is localized within the nanorod and results in its fracture because of the small aspect ratio, the thickness dimension of the nanobelt is much smaller than the lateral dimensions (Fig. 1a and b). This belt-like morphology makes lattice distortion possible during compression. The HA nanobelt can be therefore be recovered after the release of the force. Diffraction patterns of the HA nanobelt under deformation showed distinct radial spot broadening (ESI1 Fig. S5†) due to lattice distortion. The lattice distortion was directly caused by the high strain in the crystal during the compression process (ESI5 Movie†).26-28 In addition, the HA nanobelts could form multi-layered structures (Fig. 5). The obtained SAED pattern from different layers in the circle area marked as A and B [Fig. 5(a)] did not change, indicating a mutual growth orientation and matched lattice structure among different layers. The HRTEM image [Fig. 5(d)] shows a lattice distance of 3.44Å, identifying the (002) planes of single-crystal HA. To investigate the muti-layered structures of HA nanobelts in detail, several cross-sectional samples were prepared by first mixing the nanobelt sample with cold mounting epoxy resin (EPOFIX, Electron Microscopy Sciences) hardener (EPOFIX, triethylenetetramine, Microscopy Sciences). The solidified mixture was then fixed

onto the sample stage of Leica Ultracut UCT ultramicrotome and mechanically cut into transparent slices with a diamond knife. It was found that almost all of the ultrathin section samples were composed of multi-layered structures in TEM, as illustrated in Fig. 5e. The high resolution TEM image of the interface (Fig. 5f) shows clear lattice fringes, which can be indexed to the (111) plane of HA crystal. The calculation of interplanar spacing was shown in Fig. 5g, with the aid of the Digital Micrograph software. The multilayer characteristic of HA nanobelts may further enhance their flexibility. Compared to single-layered nanobelts, the multi-layered nanobelts can endure more stress during the deformation process because multi-layered structures easily slide next to each other (ESI6 Movie†) to prevent the applied stress from concentrating in one point. Similar to graphene ribbons¹⁶, the compression-bending behavior in HA nanobelts is in a platelike manner wherein layer sliding occurs and releases the in-plane strains efficiently on the neutral surface, like bending a stack of paper. It suggests that such multi-layered structure plays a significant role in determining the super flexibilility of the nanobelts.

In conclusion, we synthesized highly flexible hydroxyapatite (HA) nanobelts with uniform morphology and high aspect ratios by a one-step hydrothermal homogeneous precipitation method. More importantly, we for the first time, directly visualized the nanomechanical behaviour of individual HA nanobelts by an *in situ* nano-manipulation system under TEM. The nanobelts can be easily bent, scrolled, and stretched through seven times of cyclic compression tests, showing remarkable nanomechanical flexibility rather than fracturing. Further, nanoindentation tests were conducted, indicating that the HA nanobelt has a better resistance to deformation as well as a more reduced modulus, which is consistent with the *in situ* TEM tests. The results support the application of HA nanobelts as load-bearing implants, reinforcements in biomedical composite materials, and scaffolds for the tissue engineering.

This work was supported by National Science Foundation CAREER Award No. 1564950. R. Shahbazian-Yassar acknowledges funding from NSF DMR-1710049. Special thanks to Dr. Wen Li of China University of Petroleum for his friendly help on this work.

Conflicts of interest

There are no conflicts to declare.

Notes and references

- 1. C. Zhang, C. Li, S. Huang, Z. Hou, Z. Cheng, P. Yang, C. Peng and J. Lin, *Biomaterials*, 2010, **31**, 3374.
- 2. Z. Hou, P. Yang, H. Lian, L. Wang, C. Zhang, C. Li, R. Chai, Z. Cheng and J. Lin, *Chem.-Eur. J.*, 2009, **15**, 6973.
- 3. S. V. Dorozhkin, J. Funct. Biomater., 2010, 1, 22.
- 4. W. Suchanek and M. Yoshimura, J. Mater. Res., 1998, 13, 94.
- 5. A. C. Taş, J. Am. Ceram. Soc., 2001, 84, 295-300.
- A. J. Nathanael, S. I. Hong, T. H. Oh, Y. H. Seo, D. Singh and S. S. Han, RSC Adv., 2016, 6, 25070.
- 7. S. K. Padmanabhan, A. Balakrishnan, M.-C. Chu, Y. J. Lee, T. N. Kim and S.-J. Cho, *Particuology*, 2009, **7**, 466.

COMMUNICATION CrystEngComm

- 8. P. Franco, C. João, J. Silva and J. Borges, *Mater. Lett.*, 2012, **67**, 233
- 9. J. Holopainen and M. Ritala, J. Eur. Ceram. Soc., 2016, 36, 3219.
- 10. S. V. Dorozhkin, Acta Biomater., 2010, 6, 715.
- 11. T. J. Webster, Advances in chemical engineering, 2001, 27, 125.
- 12. B. Q. Lu, Y. J. Zhu and F. Chen, Chem.-Eur. J., 2014, 20, 1242.
- 13. J. Tao, W. Jiang, H. Pan, X. Xu and R. Tang, *J. Cryst. Growth*, 2007, **308**, 151.
- 14. T. Shokuhfar, G. K. Arumugam, P. A. Heiden, R. S. Yassar and C. Friedrich, *ACS nano*, 2009, **3**, 3098.
- 15. F. Xu, H. Ma, S. Lei, J. Sun, J. Chen, B. Ge, Y. Zhu and L. Sun, *Nanoscale*, 2016, **8**, 13603.
- 16. I. Nikiforov, D.-M. Tang, X. Wei, T. Dumitrică and D. Golberg, *Phys. Rev. Lett.*, 2012, **109**, 025504.
- 17. L. Landau, E. Lifshitz, A. Kosevich and L. Pitaevskiæi, Pergamon Press, Oxford, 1986.
- 18. H. D. Espinosa, R. A. Bernal, T. Filleter. Small, 2012, 8: 3233.
- 19. J. Vaughn and M. Kordesch, J. Vac. Sci. Technol., 2009, 27, 1058.
- 20. S. J. Pennycook, B. David, C. B. Williams. *Microsc Microanal*, 2010, **16**, 111.
- 21. W. C. Oliver and G. M. Pharr, J. Mater. Res., 2004, 19, 3.
- 22. W. C. Oliver and G. M. Pharr, J. Mater. Res., 1992, 7, 1564.
- 23. A. Nieto, B. Boesl and A. Agarwal, Carbon, 2015, 85, 299-308.
- 24. I. N. Sneddon, Int J Eng Sci, 1965, 3, 47.
- 25. H. A. Shirazi, S. Mirmohammadi, M. Shaali, A. Asnafi and M. Ayatollahi, *Polym. Test.*, 2017, **59**, 328.
- 26. T. E. Weirich, J. L. Lábár and X. Zou, Springer Science & Business Media, 2006, 211.
- 27. C. Zhang, O. Cretu, D. G. Kvashnin, N. Kawamoto, M. Mitome, X. Wang, Y. Bando, P. B. Sorokin and D. Golberg, *Nano Lett.*, 2016, **16**. 6008.
- 28. A. Popov, I. Y. Pyshmintsev, S. Demakov, A. Illarionov, T. Lowe, A. Sergeyeva and R. Valiev, *Scripta Mater.*, 1997, **37**, 1089.

Footnotes

- ‡ Electronic Supplementary Information (ESI) available at DOI: 10.1039/x0xx00000x
- **ESI1 Electronic Supplementary Information**
- ESI2 Movie: Compression test of the nanobelt (AVI)
- ESI3 Movie: Compression test of another nanobelt (AVI)
- ESI4 Movie: Compression test of the nanorod (AVI)
- ESI5 Movie: Compression test of the multi-layered nanobelt (AVI)

CrystEngComm COMMUNICATION

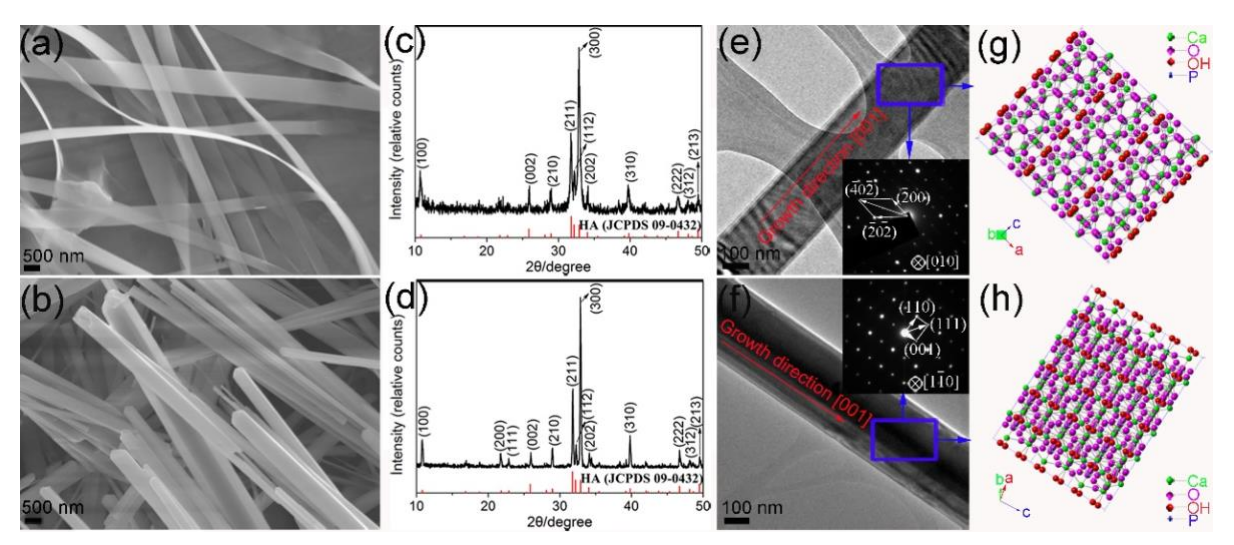


Figure 1. FE-SEM images of the synthesized products with urea (a) and acetamide (b) as pH regulator; (c-d) the corresponding XRD patterns of the products in (a-b); (e-f) TEM images of an individual nanobelt and nanorod with their SAED patterns (insets); (g-h) The crystal model of the nanobelt and nanorod in (c-d).

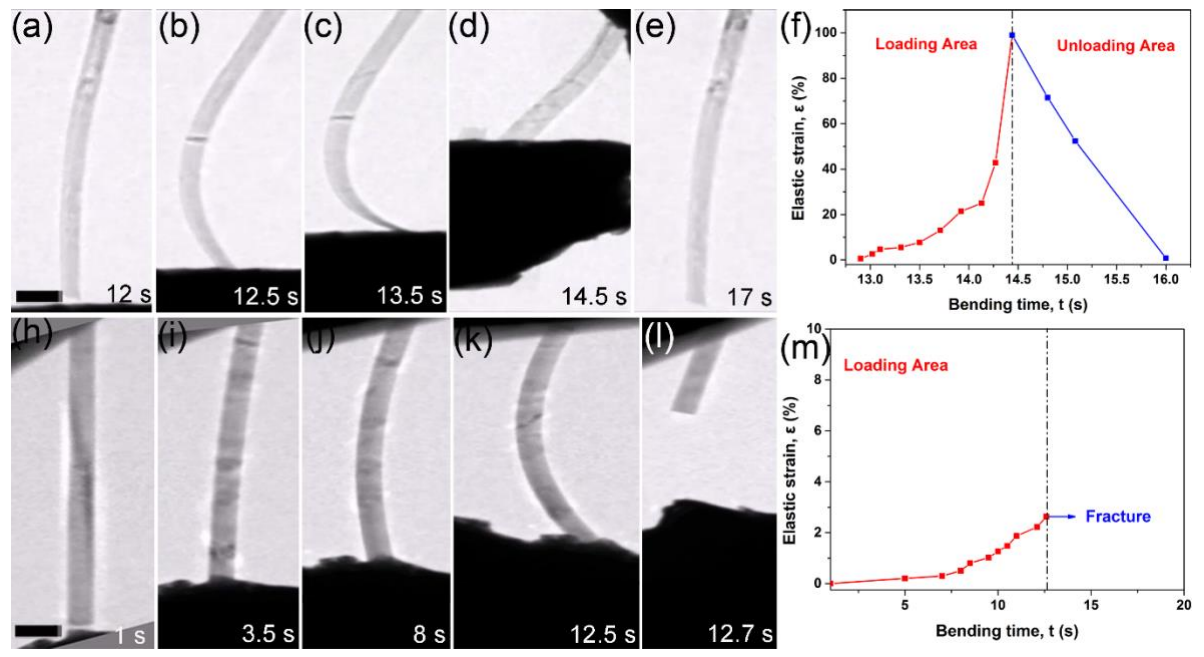


Figure 2. (a-e) Sequential morphological evolution of the HA nanobelt under the seventh severe compression cycle, and (f) the corresponding ε -t curve of the nanobelt during this process, (h-l) Sequential morphological of the HA nanorod during compression, and (m) the corresponding ε -t curve of the nanorod during this process. See ESI2 Movie† and ESI3 Movie† for details. Scale bar is 200 nm.

COMMUNICATION CrystEngComm

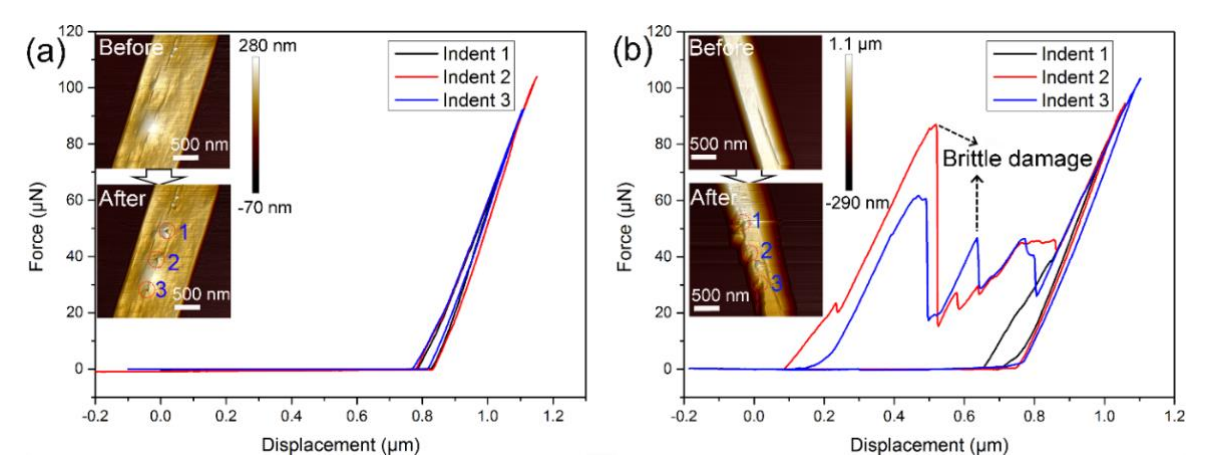


Figure 3. Representative force vs displacement curves obtained from nanoindentation test: (a) HA nanobelt, and (b) HA nanorod. The inset images are the surface morphology of the nanobelt and nanorod taken before and after the experiment in AFM.

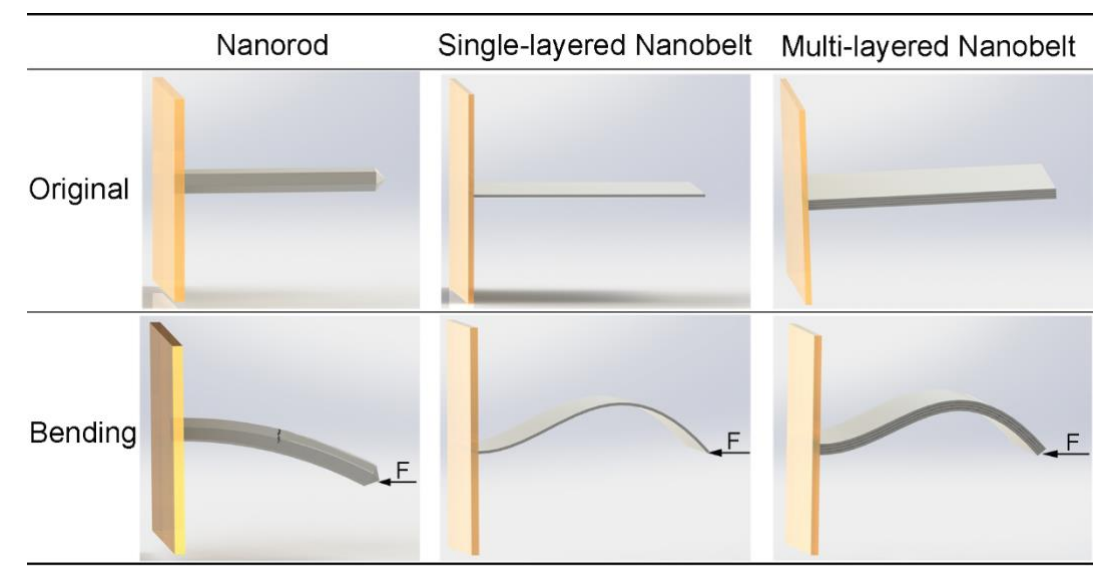


Figure 4. Compression behavior schematic of the HA nanorod, single-layered nanobelt, and multi-layered nanobelt during deformation.

CrystEngComm COMMUNICATION

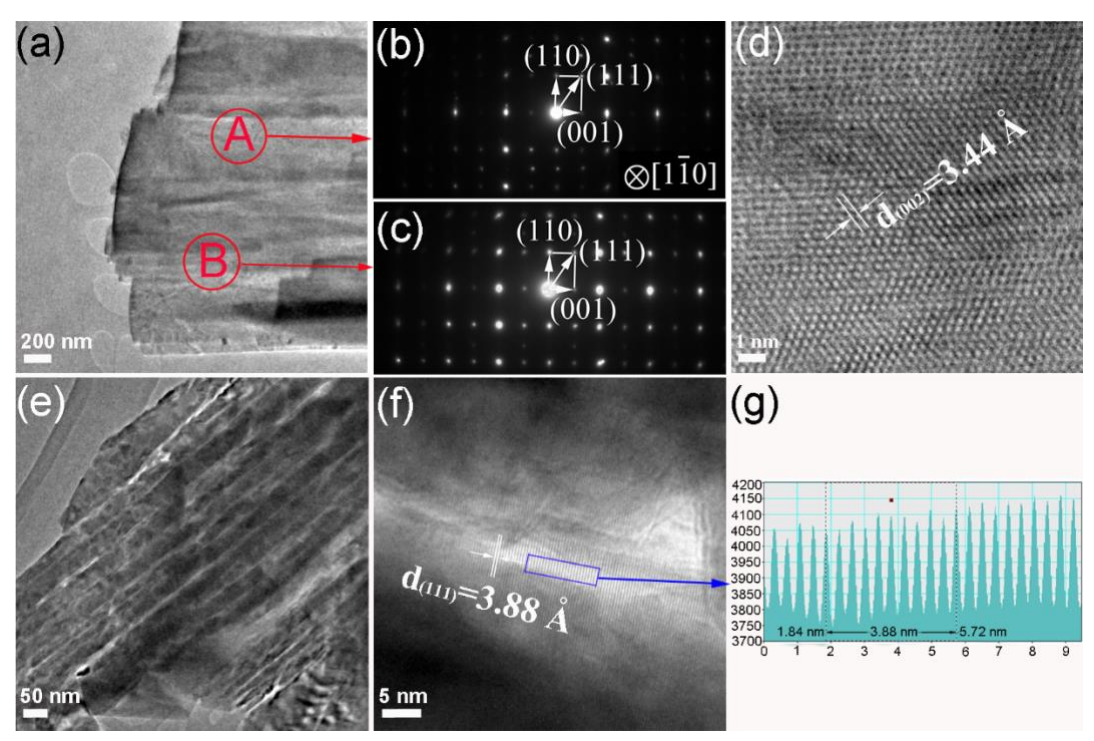


Figure 5. TEM (a) The multi-layered HA nanobelt, (b) and (c) are the SAED patterns obtained from different areas of A and B, marked with red circles in (a), (d) The HRTEM image, (e) a typical TEM image of one cross sectioned HA nanobelt slice showing the multi-layered structure, (f) the HRTEM image showing the interface between the two layers, with the corresponding calculation of interplanar spacing in (g).